geosciences

MDPI

Article

Assessing Seasonal Biogeochemical Variations in the Mun River watershed Using Water Quality Data and Geochemical Mass Balance Method

Supanut Suntikoon [1], Pee Poatprommanee [2] and Schradh Saenton [1,2,3]

[1] Environmental Science Research Center, Faculty of Science, Chiang Mai University, Chiang Mai, 50200, Thailand; supanut_suntikoon@cmu.ac.th
[2] Department of Geological Sciences, Faculty of Science, Chiang Mai University, Chiang Mai, 50200, Thailand; pee_poat@cmu.ac.th
[3] Advanced Research Center for Computational Simulation, Faculty of Science, Chiang Mai University, Chiang Mai, 50200, Thailand; schradh.saenton@cmu.ac.th
* Correspondence: schradh.saenton@cmu.ac.th

Abstract: The Mun River watershed, a vital water resource in Northeastern Thailand and a major tributary of the Mekong River, faces significant water quality challenges driven by climate change and human activities. This study examines seasonal biogeochemical variations in the watershed, with a focus on how climate fluctuations affect water quality and geochemical processes. Water samples were collected from 19 surface sites during the dry and wet seasons of 2024 and analyzed for major dissolved ions. Using the Geochemical Mass Balance method, we quantified rates of mineral weathering and biomass degradation. Our findings reveal a notable shift in hydrochemical facies from $Ca\text{-}HCO_3$ dominance in the wet season to Na-Cl dominance in the dry season, suggesting increased salinity and altered geochemical conditions. Wet season mineral weathering rates averaged 300-700 μmol m^{-2} d^{-1}, approximately 10-20 times higher than those in the dry season. The highest weathering and biomass degradation rates, ranging from 900-1200 μmol m^{-2} d^{-1}, were observed in the northern subwatersheds, likely due to intensified agricultural practices and underlying geological conditions. These results highlight the urgent need for adaptive watershed management strategies to address the growing impact of climate change on regional water quality.

Keywords: Mun River; biogeochemical variations; water quality; geochemical mass balance; climate change

Citation: To be added by editorial staff during production.

Academic Editor: Firstname Lastname

Received: date
Revised: date
Accepted: date
Published: date

1. Introduction

The Mun River watershed, a major tributary of the Mekong River, faces significant challenges in water quality and quantity, driven by both natural and anthropogenic factors. Declines in water quality have been well-documented **[1]**, alongside reductions in water availability exacerbated by climate variability and human activities **[2,3]**. These changes pose serious threats to local ecosystems and livelihoods, particularly in downstream Mekong regions **[4-6]**. Infrastructure projects, such as hydropower, exacerbate these issues by reducing biodiversity and fish productivity across the watershed **[7,8]**, while deforestation increases runoff and seasonal fluctuations in surface water **[9]**.

Agriculture dominates land use in the Mun River watershed, which is Thailand's largest cassava-producing region and one of its most water-stressed areas **[10]**. Intense rainfall, tropical cyclones, and the interplay of floods and droughts directly impact agricultural activities, particularly rice cultivation **[11,12]**. This agricultural reliance, combined with extreme precipitation events and limited water availability, intensifies pressure on the watershed's resources and compounds challenges in maintaining water

quality and quantity. Seasonal precipitation patterns further influence hydrological dynamics, with rainfall predominantly occurring during the rainy season and increasing downstream, while the dry season sees reversed patterns with reduced flow **[13]**. Climate models project that high-emission scenarios could increase temperature variability (1.45–1.54°C) and alter rainfall distribution, with wetter rainy seasons and drier pre-rainy periods **[14]**. Such shifts disrupt the hydrological cycle, exacerbate nutrient depletion through soil erosion, and amplify seasonal fluctuations in surface water quality, particularly under the tropical monsoonal climate **[15-18]**.

Biogeochemical cycles, essential for watershed health, reflect interactions between climate patterns, geology, and anthropogenic influences. Seasonal shifts in these cycles are key indicators of watershed resilience, particularly between dry and wet seasons. The chemical weathering of silicate and carbonate minerals drives carbon cycling, influencing atmospheric CO_2 sequestration and global climate regulation **[19-23]**. Understanding mineral weathering rates within the Mun River watershed is critical for both local water quality management and broader insights into carbon cycling under changing land use and climate conditions. Anthropogenic drivers, such as agriculture **[24]**, industrialization **[25]**, land-use changes **[26,27]**, deforestation, and urbanization **[28]**, significantly impact biogeochemical processes. For example, iron isotope geochemistry reveals that iron sources derive from both natural weathering and urban activities **[29]**, while seasonal contributions of Rare Earth Elements (REEs) vary, with soil materials dominating in the dry season and rock weathering becoming prominent during the rainy season **[30]**.

Expanding agricultural irrigation and hazardous industries, particularly upstream, have disrupted flow and sediment transport, contributing to water quality degradation**[31-33]**. Additionally, rice cultivation in downstream areas has increased nutrient discharge, while poorly consolidated sandy soils amplify sediment load and water quality issues during intense monsoonal rainfall **[34-36]**. While Geographic Information System (GIS) and remote sensing methods are effective for mapping surface-level changes, they cannot capture subsurface flows that significantly influence biogeochemical cycles **[37-39]**. Supplementary techniques are thus necessary to fully understand these dynamics.

The Geochemical Mass Balance (GMB) method offers an integrated framework for assessing biogeochemical processes by incorporating biomass, geology, and hydrology **[40]**. Though widely applied elsewhere, GMB has not been utilized in the Mun River watershed, leaving gaps in understanding the spatiotemporal variations in mineral weathering, biomass degradation, and water type classifications. Weathering rates are particularly relevant as they contribute to terrestrial CO_2 sequestration, mitigating climate change impacts. Silicate weathering, for instance, plays a substantial role in CO_2 consumption **[41]**. This study applies the GMB method to quantify seasonal variations in mineral weathering and biomass degradation in the Mun River watershed, aiming to address knowledge gaps and provide actionable insights. By analyzing water samples from dry and wet seasons, the study seeks to inform adaptive watershed management strategies, enhancing climate resilience and sustainability for the watershed and its downstream ecosystems **[42]**.

2. Materials and Methods

2.1. Study area

The Mun River watershed (Figure 1), located in Northeastern Thailand, spans approximately 71,059 square kilometers and serves as a key tributary of the Mekong River. It plays a crucial role in regional hydrology, extending over 900 km and encompassing 11 provinces [43]. Land use in the watershed is predominantly agricultural, with about 80% of the area dedicated to cultivation, supported by widespread fertilizer and pesticide use. Annual fertilizer use reaches 20,000 tons, with pesticides contributing several thousand tons [44,45].

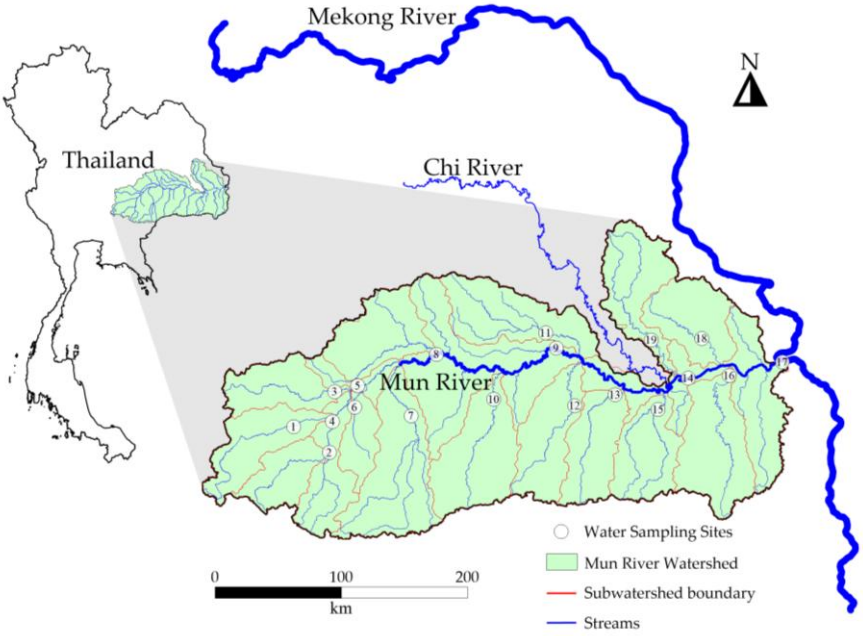

Figure 1. Location of the Mun River watershed and water sampling sites.

Population density is highest in the middle Mun region, averaging 150 people per square kilometer, with densities ranging from 37 to 601 people per square kilometer [46]. The watershed experiences a tropical monsoon climate, characterized by a dry season (November to April) and a wet season (May to October). Rainfall increases from the upper western watershed, receiving around 870 mm annually, to the lower eastern region, where precipitation averages 1,758 mm [17]. The Asian monsoon system primarily drives precipitation, with wet season rainfall impacting the middle to lower reaches [47].

Geologically, the watershed is dominated by sedimentary formations such as sandstone, siltstone, and evaporites, which heavily influence water chemistry. The northern watershed features quartzitic sandstone, siltstone, and evaporite-rich Maha Sarakham formations, interspersed with Pre-Jurassic volcanic rocks and granites. In contrast, basaltic formations are prevalent in the southern watershed, particularly along the right tributaries of the Mun River. The Chi River, the largest tributary, adds hydrological complexity. These geological and climatic factors (Figure 2) establish the Mun River watershed as an ideal site for studying biogeochemical processes [48].

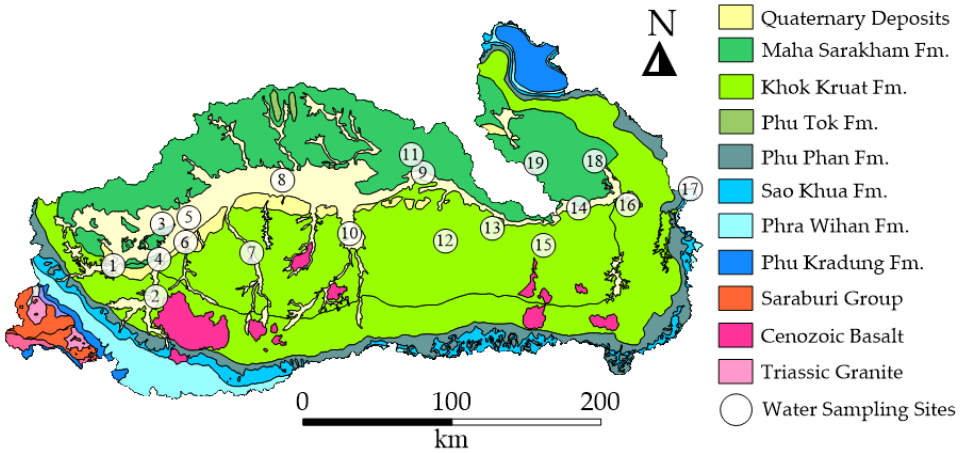

Figure 2. Geologic units underlying the Mun River watershed.

2.2. Sample collection and analysis

Water samples were collected from 19 surface water sites during mid-March (dry season) and mid-August (wet season) of 2024, ensuring comprehensive representation across the watershed. Sampling locations were carefully selected to represent individual subwatersheds, identified and delineated using a Digital Elevation Model (DEM) from the Shuttle Radar Topography Mission (SRTM), available via the USGS EarthExplorer website (https://earthexplorer.usgs.gov). This approach enabled the division of the large Mun River watershed into 19 smaller subwatersheds, each characterized by unique hydrological and topographical conditions. The selected sites, illustrated in Figure 1, accounted for diverse land-use types and ensured accessibility while being located near stream gaging stations with discharge data. Sampling near subwatershed outlets facilitated accurate calculations of dissolved species export.

Water samples were collected in pre-cleaned polyethylene bottles, stored on ice during transport, and refrigerated at 4°C (±2°C) until laboratory analysis. Field measurements included pH, electrical conductivity (EC), oxidation-reduction potential (ORP), and alkalinity. In the laboratory, water samples were filtered through 0.45-μm membrane filters before chemical analysis. Major cations (Na^+, K^+, Ca^{2+}, Mg^{2+}, $Si(O_2)(aq)$) were quantified using inductively coupled plasma mass spectrometry (ICP-MS), and anions $\left(Cl^-, SO_4^{2-}, NO_3^-\right)$ were measured via ion chromatography. Carbonate concentrations and water hardness were determined by titration, and total dissolved solids (TDS) were measured gravimetrically. Ion balance was verified using Aquachem software, maintaining charge balance errors below 5%, a standard threshold in hydrochemical studies.

2.3. Hydrochemical facies

Hydrochemical facies were analyzed using Aquachem software, with Stiff diagrams employed to visualize the ionic composition of water samples (in meq L^{-1}) and map the spatial distribution of water types across the watershed during both seasons. Piper diagrams further illustrated seasonal shifts in hydrochemical characteristics, providing insights into patterns such as salinity increases and cation exchange. These visual tools facilitated the interpretation of seasonal variability in water chemistry.

2.4. Geochemical Mass Balance (GMB) analysis

In line with earlier recommendations emphasizing the importance of watershed size to minimize the effects of unaccounted deep groundwater flow [49], this study applied the Geochemical Mass Balance (GMB) model to individual subwatersheds. By focusing on smaller drainage areas, the model more accurately captures biogeochemical processes, as inputs and outputs are less influenced by extensive residence times. The GMB model balances dissolved species inputs (from weathering and biomass degradation) with outputs via runoff and secondary mineral formation. Solute fluxes were resolved using a matrix of linear equations, providing weathering and biomass change rates in micromoles per square meter per day (μmol m^{-2} d^{-1}). Minerals of particular interest included halite, feldspar, biotite, and garnet. Rainfall and evaporation rates were excluded from this analysis.

The mass balance equation used is as follows [49,50]:

$$\sum_{j=1}^{k} \alpha_j \beta_{i,j} = \Delta m_c \quad \text{for } c = 1, \ldots, n \tag{1}$$

Where:

k : Number of unknown variables,
j : Index for minerals or biomass undergoing weathering,
α : Weathering rate of mineral or biomass j (moles per area per time),
β : Stoichiometric coefficient for ion c in mineral or biomass j,
Δm_c : Flux change rate of ion c (moles per area per time).

3. Results and discussion

3.1. Physiochemical parameters

Seasonal variations in temperature and pH provide insights into the hydrological and geochemical dynamics of the Mun River watershed. During the dry season, temperatures ranged from 25.60°C to 31.80°C, with a mean of 28.23°C, while in the wet season, temperatures ranged from 25.00°C to 33.00°C, averaging slightly higher at 28.63°C (Table 1). The difference in mean temperatures between the seasons was statistically insignificant ($p = 0.538$), indicating that temperature consistently influences water chemistry across seasons.

Table 1. Seasonal variations in physicochemical parameters and major ion concentrations in the Mun River were analyzed. P-values were calculated using a two-sample t-test (or the Mann-Whitney U test for non-normal distributions) to assess seasonal differences. Statistically significant p-values ($p < 0.05$) are highlighted in red to emphasize notable seasonal variations.

Parameter	Season	Min	Max	Mean	Median	SD[1]	p-value
T (°C)	Dry	25.60	31.80	28.23	28.30	1.62	0.538
	Wet	25.00	33.00	28.63	29.00	2.78	
pH	Dry	6.70	7.80	7.44	7.60	0.31	0.027
	Wet	6.40	7.70	6.97	6.90	0.45	
Cond ($\mu S\ cm^{-1}$)	Dry	78.00	2449.00	490.53	291.00	536.26	0.027
	Wet	32.00	2357.00	313.26	140.00	517.71	
TDS ($mg\ L^{-1}$)	Dry	56.34	1332.07	312.44	198.67	304.77	0.009
	Wet	26.19	1166.50	179.33	84.85	258.19	
Alkalinity ($mg\ L^{-1}\ CaCO_3$)	Dry	6.00	164.36	60.34	51.79	43.13	0.153
	Wet	4.50	150.94	39.51	21.48	39.54	
DO ($mg\ L^{-1}$)	Dry	4.00	8.20	6.40	6.50	1.13	< 0.001
	Wet	3.00	5.90	4.63	4.70	0.76	
Flowrate ($m^3\ s^{-1}$)	Dry	0.00	101.42	14.27	0.75	29.65	< 0.001
	Wet	1.60	471.70	100.99	44.60	132.64	
Na^+ ($mg\ L^{-1}$)	Dry	6.35	369.60	62.87	31.58	85.32	0.068
	Wet	2.12	326.23	35.87	13.65	71.55	
K^+ ($mg\ L^{-1}$)	Dry	1.32	14.05	5.21	5.12	3.29	0.153
	Wet	1.11	10.10	3.62	2.41	2.98	
Ca^{2+} ($mg\ L^{-1}$)	Dry	1.29	62.50	19.24	17.48	15.18	0.153
	Wet	1.78	62.40	12.60	6.20	15.87	
Mg^{2+} ($mg\ L^{-1}$)	Dry	0.84	16.18	5.43	4.49	3.80	0.068
	Wet	0.50	13.99	3.24	1.81	3.54	
$SiO_2(aq)$ ($mg\ L^{-1}$)	Dry	4.59	13.47	9.65	9.98	2.65	0.009
	Wet	3.32	13.94	7.41	6.50	3.57	

Cl^- (mg L^{-1})	Dry	9.87	668.55	104.72	49.86	152.79	0.027
	Wet	3.77	603.01	57.11	13.75	132.29	
HCO_3^- (mg L^{-1})	Dry	7.32	200.39	74.05	63.14	52.73	0.306
	Wet	5.49	184.03	48.65	31.14	48.02	
SO_4^{2-} (mg L^{-1})	Dry	1.08	18.34	8.06	5.64	6.14	0.538
	Wet	1.30	28.36	6.39	4.03	6.73	
NO_3^- (mg L^{-1})	Dry	0.21	8.01	1.98	1.06	2.24	0.395
	Wet	0.30	2.71	1.07	0.62	0.90	

[1]SD: Standard Deviation

In contrast, pH levels exhibited significant seasonal variability. The dry season showed slightly alkaline conditions, with pH ranging from 6.70 to 7.80 (mean = 7.44), while the wet season shifted toward neutral pH, ranging from 6.40 to 7.70 (mean = 6.97) (Table 1, $p = 0.027$). This seasonal difference is attributed to increased runoff and dilution during the wet season, which lowers pH by introducing organic acids and rainwater. These fluctuations in pH can influence mineral solubility and biological processes, underscoring its role in geochemical and ecosystem health [25].

Electrical conductivity (Cond) and total dissolved solids (TDS) serve as indicators of ion concentration, reflecting geochemical processes. Conductivity in the dry season ranged from 78.00 to 2449.00 μS cm^{-1} (mean = 490.53 μS cm^{-1}), while wet-season values were significantly lower, ranging from 32.00 to 2357.00 μS cm^{-1} (mean = 313.26 μS cm^{-1}, $p = 0.027$). TDS showed similar seasonal reductions, with dry-season values ranging from 56.34 to 1332.07 mg L^{-1} (mean = 312.44 mg L^{-1}) and wet-season values from 26.19 to 1166.50 mg L^{-1} (mean = 179.33 mg L^{-1}, $p = 0.009$). These trends highlight the role of monsoonal rains in diluting dissolved ions, particularly in agricultural areas where salinity during the dry season may affect soil and crop health.

Alkalinity, dissolved oxygen (DO), and flow rate further illustrate seasonal impacts on water quality. Alkalinity was higher in the dry season (mean = 60.34 mg L^{-1} $CaCO_3$) compared to the wet season (mean = 39.51 mg L^{-1}), though the difference was not statistically significant ($p = 0.153$). Higher dry-season alkalinity suggests a greater concentration of dissolved carbonate species due to lower flow rates and evaporation. DO levels, however, varied significantly between seasons, with higher concentrations in the dry season (mean = 6.40 mg L^{-1}) compared to the wet season (mean = 4.63 mg L^{-1}, $p < 0.001$), likely due to increased photosynthesis in clearer waters during the dry season and higher organic decomposition during the wet season. Flow rates showed dramatic seasonal variation, with dry-season flow ranging from 0.00 to 101.42 m^3 s^{-1} (mean = 14.27 m^3 s^{-1}) and wet-season flow ranging from 1.60 to 471.70 m^3 s^{-1} (mean = 100.99 m^3 s^{-1}, $p < 0.001$), emphasizing the impact of monsoonal rainfall on hydrological dynamics [27].

3.2. Major dissolved species chemistry

The concentrations of major dissolved species, including Na^+, K^+, Ca^{2+}, Mg^{2+}, $SiO_2(aq)$, Cl^-, HCO_3^-, SO_4^{2-}, and NO_3^-, exhibit notable seasonal variability, reflecting the combined influence of hydrological, geochemical, and anthropogenic factors. These species were generally higher in the dry season due to reduced river flow and increased evaporation, which concentrate dissolved components. This trend aligns with previous studies in the region, where agricultural, industrial, and domestic discharges also contributed to elevated ion concentrations during low-flow periods [51].

Cations: Sodium (Na^+) concentrations ranged from 6.35 to 369.60 mg L^{-1} (mean = 62.87 mg L^{-1}) during the dry season and from 2.12 to 326.23 mg L^{-1} (mean = 35.87 mg L^{-1})

during the wet season (Table 1). This seasonal increase ($p = 0.068$) is attributed to the weathering of sodium-rich minerals like halite and plagioclase feldspar, which are abundant in the northern subwatersheds, and to evaporative concentration during the dry season. Elevated Na^+ levels may contribute to long-term soil salinity issues, emphasizing the need for targeted salinity management, particularly in northern agricultural regions [1].

Potassium (K^+) concentrations followed a similar seasonal pattern, with dry-season levels ranging from 1.32 to 14.05 mg L^{-1} (mean = 5.21 mg L^{-1}) and wet-season levels from 1.11 to 10.10 mg L^{-1} (mean = 3.62 mg L^{-1}) (Table 1). While this difference was not statistically significant ($p = 0.153$), it reflects the contribution of feldspar and mica weathering. Similarly, calcium (Ca^{2+}) and magnesium (Mg^{2+}) concentrations were higher in the dry season, with Ca^{2+} ranging from 1.29 to 62.50 mg L^{-1} (mean = 19.24 mg L^{-1}) and Mg^{2+} from 0.84 to 16.18 mg L^{-1} (mean = 5.43 mg L^{-1}) (Table 1). These trends suggest intensified carbonate and silicate weathering under lower flow conditions. Dissolved silica ($SiO_2(aq)$), derived from silicate mineral weathering, showed a comparable seasonal pattern, with dry-season concentrations averaging 9.65 mg L^{-1} compared to 7.41 mg L^{-1} in the wet season ($p = 0.009$). These results underscore the role of hydrological variability in regulating weathering processes.

Anions: Seasonal variation in major anions—chloride (Cl^-), bicarbonate (HCO_3^-), sulfate (SO_4^{2-}), and nitrate (NO_3^-)—was also observed across the watershed. Chloride concentrations were significantly higher in the dry season, ranging from 9.87 to 668.55 mg L^{-1} (mean = 104.72 mg L^{-1}), compared to the wet season (mean = 57.11 mg L^{-1}, $p = 0.027$) (Table 1). This increase is primarily linked to evaporite dissolution and is influenced by anthropogenic inputs, such as agricultural runoff. Many dry-season samples exceeded the World Health Organization (WHO) drinking water guideline for chloride (7 mg L^{-1}) [52], highlighting salinity issues in areas dominated by evaporite-rich formations.

Sulfate (SO_4^{2-}) concentrations followed a similar seasonal trend, with dry-season levels ranging from 1.08 to 18.34 mg L^{-1} (mean = 8.06 mg L^{-1}) and wet-season levels from 1.30 to 28.36 mg L^{-1} (mean = 6.39 mg L^{-1}) (Table 1). Although the difference was not statistically significant ($p = 0.538$), sulfate levels are influenced by both natural sulfide oxidation and anthropogenic sources, including gypsum dissolution and agricultural runoff [53]. Bicarbonate (HCO_3^-) levels showed minimal seasonal variation, averaging 74.05 mg L^{-1} in the dry season and 48.65 mg L^{-1} in the wet season. This stability reflects the buffering effect of carbonate weathering, which sustains alkalinity across seasons.

Nitrate (NO_3^-) concentrations were consistently low, with dry-season levels averaging 1.98 mg L^{-1} and wet-season levels 1.07 mg L^{-1} (Table 1). The seasonal difference was not statistically significant ($p = 0.395$), and nitrate concentrations remained well below the WHO guideline of 50 mg L^{-1} [52], This suggests limited agricultural nitrate input, possibly mitigated by dilution during the wet season.

These seasonal variations in dissolved species concentrations and physicochemical parameters are visually illustrated in Figure 3, providing a comprehensive overview of the biogeochemical processes shaping water quality within the Mun River watershed.

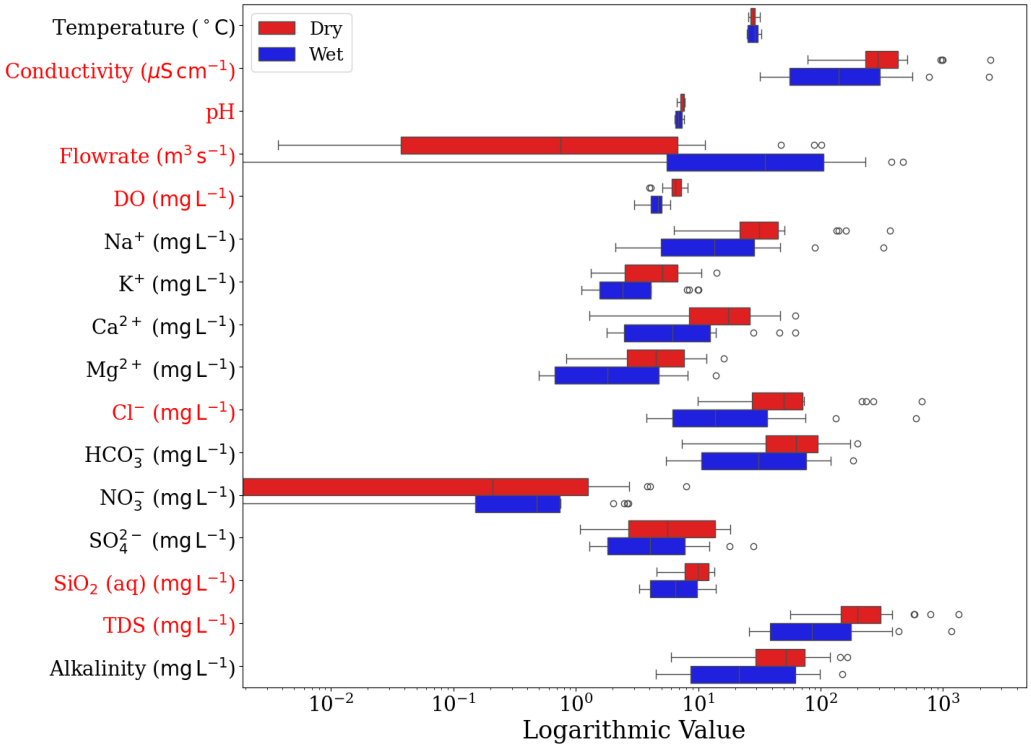

Figure 3. Comparison of physicochemical parameters and major ion concentrations in dry and wet seasons (logarithmic scale) for the Mun River. Parameters with significant seasonal differences ($p < 0.05$) are highlighted in red on the y-axis.

3.3 Hydrochemical facies, water type shifts, and spatial distribution

The Piper diagram (Figure 4) and Stiff diagrams (Figure 5) collectively illustrate seasonal and spatial shifts in hydrochemical facies across the Mun River watershed. During the dry season, Na-Cl water types dominate, reflecting the concentration of dissolved ions due to reduced flow rates and increased evaporation. In contrast, the wet season is characterized by a predominance of Ca-HCO_3 facies (Table 2), driven by the dilution effects of higher precipitation and enhanced weathering of carbonate minerals. This seasonal variability aligns with previous findings, where Na^+ and Cl^- were identified as the dominant ions, following the cation order $Na^+ > Ca^{2+} > Mg^{2+} > K^+$ and the anion order $Cl^- > HCO_3^- > SO_4^{2-} > NO_3^-$, indicating a natural prevalence of Na-Cl facies [46].

The overall hydrochemical type of the Mun River, classified as Na-Ca-Cl-HCO_3, is influenced by both natural geochemical processes—primarily evaporite dissolution and silicate weathering—and anthropogenic inputs such as agricultural runoff and wastewater discharge. These factors result in elevated ion concentrations during the dry season, while wet-season flow rates dilute these ions, leading to the dominance of Ca-HCO_3 facies [41,54].

Table 2. Percent error (Δ%) of chemical analyses and corresponding hydrochemical facies. The percent error (Δ%) represents the relative difference between total cations and anions in milliequivalents per liter (meq L^{-1}), with acceptable values generally within ±5%. Hydrochemical facies are shown for both wet and dry seasons.

	Δ%		Facies	
Sample	**Wet**	**Dry**	**Wet**	**Dry**
1	1.20	0.52	Ca-HCO_3	Ca-HCO_3
2	1.34	1.44	Na-HCO_3	Na-Cl
3	1.70	2.73	Na-Cl	Na-Cl

4	1.02	1.21	$Na\text{-}HCO_3$	Na-Cl
5	1.23	1.15	Na-Cl	Na-Cl
6	1.11	2.11	$Ca\text{-}HCO_3$	$Na\text{-}HCO_3$
7	1.01	0.23	$Na\text{-}HCO_3$	Na-Cl
8	1.23	0.64	Na-Cl	Na-Cl
9	1.44	1.64	Na-Cl	Na-Cl
10	1.43	3.52	$Na\text{-}HCO_3$	Ca-Cl
11	1.76	0.37	Na-Cl	Na-Cl
12	2.57	4.82	$Na\text{-}HCO_3$	Na-Cl
13	1.75	0.41	Na-Cl	Na-Cl
14	1.17	2.48	Na-Cl	$Na\text{-}HCO_3$
15	4.38	8.55	$Na\text{-}HCO_3$	$Ca\text{-}HCO_3$
16	4.23	1.33	Ca-Cl	$Ca\text{-}HCO_3$
17	2.52	2.15	$Ca\text{-}HCO_3$	$Ca\text{-}HCO_3$
18	1.20	0.52	$Ca\text{-}HCO_3$	$Ca\text{-}HCO_3$
19	1.34	1.44	$Na\text{-}HCO_3$	Na-Cl

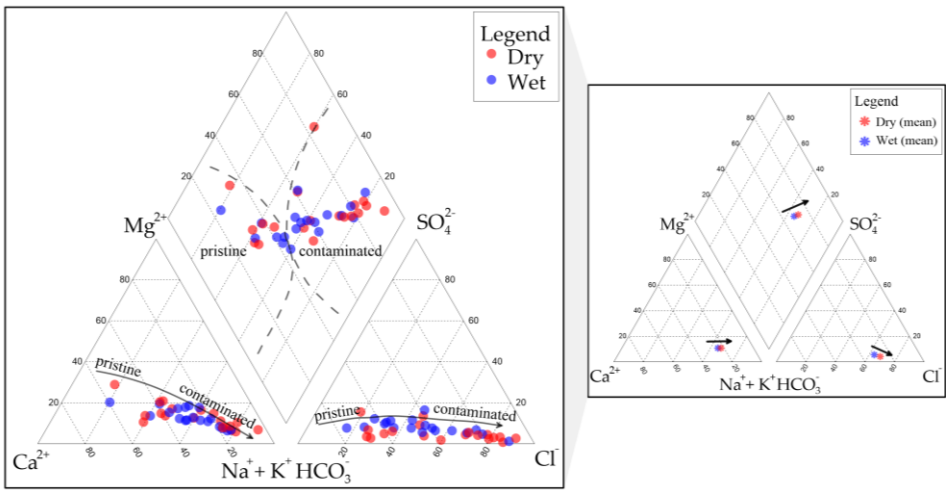

Figure 4. Piper diagram illustrating the hydrochemical facies of all collected samples across dry and wet seasons (left) and the average seasonal shifts in hydrochemical facies (right). Arrows in the right diagram depict the transition from wet-season water types (e.g., calcium bicarbonate) to dry-season water types (e.g., sodium chloride), emphasizing the seasonal evolution of water chemistry.

Stiff diagrams (Figure 5) further highlight the geographic variation in water chemistry. In the dry season (Figure 5a), larger Stiff polygons indicate higher dissolved ion concentrations due to geological factors, such as evaporite dissolution and silicate weathering, as well as agricultural runoff [55]. Conversely, in the wet season (Figure 5b), smaller Stiff diagrams reflect the dilution effects of increased precipitation and runoff, particularly in the southern subwatersheds. These regions, which shift from $Ca\text{-}HCO_3$ to Na-Cl water types during the dry season, are especially vulnerable to anthropogenic influences, including fertilizer application and wastewater inputs.

The Piper diagram also highlights differences between pristine and contaminated water types. Pristine waters typically plot in the $Ca\text{-}HCO_3$ region, indicating minimal anthropogenic influence, while contaminated waters plot in the Na-Cl domain. The more pronounced shift toward contaminated water types in the dry season underscores the impact of agricultural and urban activities on water quality. Understanding these seasonal and spatial patterns is essential for effective watershed management, particularly in

mitigating salinity issues and ensuring sustainable water quality for drinking and irrigation.

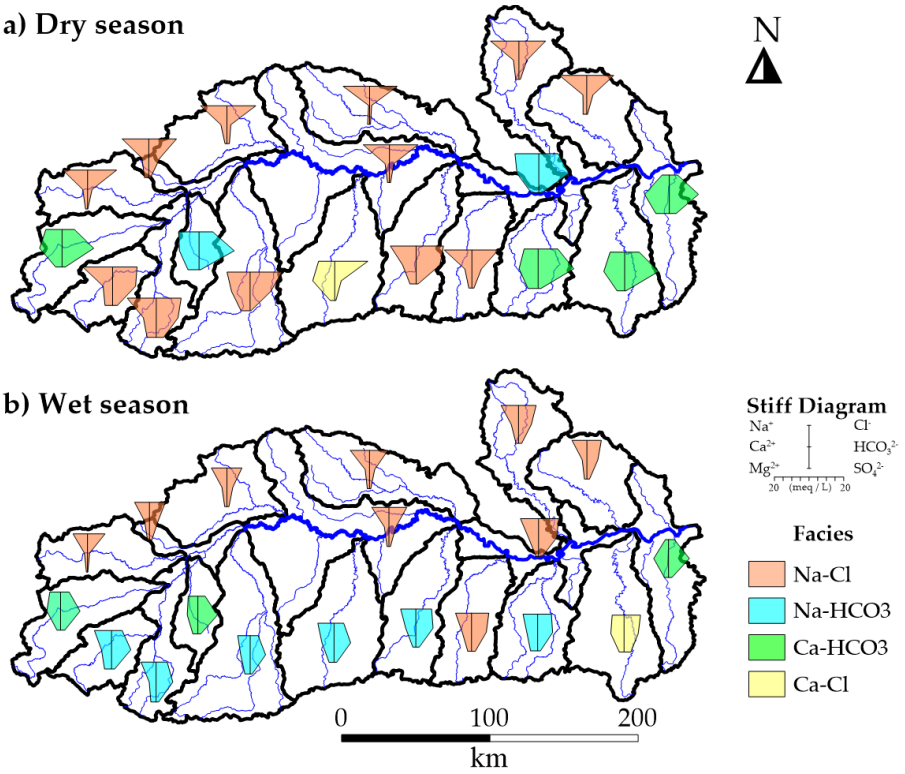

Figure 5. Stiff diagrams illustrating the spatial distribution of water types across all subwatersheds during the dry season (a) and wet season (b). The Stiff diagram legend represents the relative concentrations of major cations (Na^+, K^+, Ca^{2+}, Mg^{2+}) and anions (Cl^-, HCO_3^-, SO_4^{2-}), with the size and shape of each polygon reflecting the ionic composition and total dissolved solids at each sampling location.

3.4 Mineral weathering and biomass degradation

Rock samples from key formations within the Mun River watershed, including the Phra Wihan and Sao Khua Formations, were analyzed using X-ray Diffractometry (XRD) to determine their mineral composition (Table 3). Key minerals identified—quartz, halite, feldspar, garnet, biotite, and vermiculite—significantly contribute to the weathering processes that influence water chemistry. These minerals were used as input data for the geochemical mass balance (GMB) model, which calculates weathering rates based on stoichiometric relationships and mass flux data.

Table 3. Rock-forming minerals and biomass for Geochemical Mass Balance calculations

Mineral	Chemical Formula	Mineral weathering rate or biomass degradation rate ($\mu mol\ m^{-2}\ d^{-1}$)
Quartz	SiO_2	α_1
Halite	NaCl	α_2
Feldspar	$Na_{0.68}Ca_{0.32}Al_{1.32}Si_{2.68}O_8$	α_3
Garnet	$Ca_{0.2}Mg_{0.5}Mn_{0.2}Fe_{2.1}Al_2Si_3O_{12}$	α_4
Biotite	$K_{0.85}Na_{0.02}(Mg_{1.2}Fe_{1.3}Al_{0.45})(Al_{1.2}Si_{2.8})O_{10}(OH)_2$	α_5

Vermiculite	$K_{0.25}Na_{0.06}Ca_{0.016}(Mg_{1.1}Fe_{1.6}Al_{0.45})(Al_{1.2}Si_{2.8})O_{10}(OH)_2$	α_6
Biomass [1]	$Na_xMg_yCa_zK_w$	α_7

[1] Variables x, y, z, and w in the biomass formula vary depending on the watershed and season and are determined through inverse modeling.

Weathering and biomass degradation rates were estimated through a system of linear equations incorporating observed mass fluxes and mineral stoichiometry. This system, solved using optimization software such as PEST [56], enabled precise calculations of mineral weathering and biomass degradation rates across the watershed. Biomass degradation rates provide insights into nutrient cycling: a positive rate indicates ion release from decaying plant matter, while a negative rate reflects nutrient absorption by growing vegetation, highlighting its role in nutrient uptake and retention [40].

3.5 Geochemical mass balance calculations

3.5.1 Results from GMB analysis

Geochemical mass balance (GMB) calculations for the Mun River watershed were conducted using water quality data, focusing on major ions such as Na^+, Ca^{2+}, Mg^{2+}, K^+, and $SiO_2(aq)$. These ions, classified as conservative species due to their low likelihood of reprecipitation or loss, originate from the weathering of rock-forming minerals and biomass degradation within the study area. The elemental flux of each species, expressed in μmol m^{-2} d^{-1}, was calculated using the equation:

$$\Delta m_c = \frac{[C] \times Q}{A} \quad (2)$$

Where:

Δm_c : Elemental flux of species c,

[C] : Concentration of species c in μmol m^{-3},

Q : Stream discharge at the sampling point in m^3 d^{-1},

A : Watershed area in m^2.

The GMB calculations expanded upon this flux equation by incorporating the stoichiometric relationships of minerals and biomass into a linear system of equations:

$$A\vec{x} = \vec{b}$$

$$\begin{matrix} \text{Na}: \\ \text{Mg}: \\ \text{Ca}: \\ \text{K}: \\ \text{SiO}_2: \end{matrix} \begin{bmatrix} 0 & 1 & 0.68 & 0 & 0.02 & 0.06 & x \\ 0 & 0 & 0 & 0.5 & 1.2 & 1.1 & y \\ 0 & 0 & 0.32 & 0.2 & 0 & 0.016 & z \\ 0 & 0 & 0 & 0 & 0.85 & 0.25 & w \\ 1 & 0 & 2.68 & 3 & 2.8 & 2.8 & 0 \end{bmatrix}_{5\times7} \begin{bmatrix} \alpha_1 \\ \alpha_2 \\ \alpha_3 \\ \alpha_4 \\ \alpha_5 \\ \alpha_6 \\ \alpha_7 \end{bmatrix}_{7\times1} = \begin{bmatrix} \Delta m_{Na} \\ \Delta m_{Mg} \\ \Delta m_{Ca} \\ \Delta m_K \\ \Delta m_{SiO_2} \end{bmatrix}_{5\times1} \quad (3)$$

Where:

Matrix A contains stoichiometric coefficients derived from XRD analyses of minerals and biomass (Table 3).

Vector $\vec{x}$ includes unknown rates (α_1–α_6) for mineral weathering of quartz, halite, feldspar, garnet, biotite, and vermiculite, and α_7 for biomass degradation.

Vector $\vec{b}$ represents observed flux values for dissolved ions (Na^+, Mg^{2+}, Ca^{2+}, K^+, and $SiO_2(aq)$) from field data.

The system involved 11 unknowns and 5 known values, requiring advanced numerical methods for solution. The PEST optimization tool was used to iteratively minimize errors between observed and modeled fluxes, enabling precise calculations of mineral weathering and biomass degradation rates for each subwatershed.

"…Please explain the detail numerical methods used here…"

Results from these calculations, summarized in Table 4, highlight the spatial variability of geochemical processes. The mass fluxes of major ions Na^+, Mg^{2+}, Ca^{2+}, K^+, and $SiO_2(aq)$ discharged from the watershed showed clear seasonal distinctions, influenced by both hydrological and geological factors. Minerals such as feldspar, halite, and garnet—highly susceptible to chemical weathering—were identified as key contributors to these fluxes. These findings underscore the significant interplay between geology and hydrology in shaping weathering and biomass processes across the watershed.

Table 4. Calculation of elemental mass fluxes for geochemical mass balance.

a). Dry season

	Area	Flowrate	Concentration (mg L^{-1})					Elemental Flux (μmol m^{-2} d^{-1})				
Sample	(km^2)	m^3 s^{-1}	Na^+	K^+	Ca^{2+}	Mg^{2+}	$SiO_2(aq)$	Na^+	K^+	Ca^{2+}	Mg^{2+}	$SiO_2(aq)$
1	3420	0.9223	38.82	7.65	46.92	8.07	7.78	39.33	4.56	27.28	7.73	3.02
2	2319	0.3968	39.52	10.6	10.93	5.29	10.51	25.4	4.01	4.03	3.22	2.59
3	2888	0.0373	369.6	6.9	62.5	16.18	13.47	17.95	0.2	1.74	0.74	0.25
4	2898	0.0037	26.81	8.23	10.4	4.49	12.23	0.13	0.02	0.03	0.02	0.02
5	1061	0.0373	134.8	14.05	29.99	11.6	8.02	17.82	1.09	2.28	1.45	0.41
6	1654	0.0373	26.29	5.12	22.05	7.55	11.25	2.23	0.26	1.07	0.61	0.37
7	5934	0.2240	26.6	5.21	18.64	5.5	11.94	3.77	0.43	1.52	0.74	0.65
8	3666	9.2113	213.7	5.08	43.3	8.44	13.26	2008.3	28.2	234.5	75.4	47.9
9	7869	11.4092	141.2	6.07	27.64	7.88	11.92	765.7	19.4	86.4	40.6	24.9
10	4966	0.0373	21.51	2.57	25.58	3.23	4.87	0.61	0.04	0.41	0.09	0.05
11	4443	0.0037	36.09	1.74	1.29	1.47	4.59	0.11	0	0	0	0.01
12	3803	3.2387	6.68	1.53	3.06	0.84	7.81	21.36	2.87	5.61	2.56	9.56
13	3376	47.0710	37.13	3.52	8.29	2.17	7.29	1944.82	108.49	249.18	107.6	146.17
14	2681	88.4194	-	-	-	-	-	-	-	-	-	-
15	3360	4.2742	8.37	6.75	9.94	3.21	12.59	39.98	18.97	27.26	14.53	23.03
16	4840	2.9523	6.35	6.31	7.95	1.75	7.93	14.54	8.51	10.45	3.8	6.96
17	4041	101.419	-	-	-	-	-	-	-	-	-	-
18	3493	0.6961	31.58	1.32	3.75	2.21	7.49	23.64	0.58	1.61	1.56	2.15
19	3878	0.7467	50.74	1.48	8.49	3	12.67	36.7	0.63	3.53	2.05	3.51
Mun [1]	70589	101.419	24.08	3.33	16.95	3.62	7.50	129.97	10.57	52.50	18.50	15.51

b). Wet season

	Area	Flowrate	Concentration (mg L^{-1})					Elemental Flux (μmol m^{-2} d^{-1})				
Sample	(km^2)	m^3 s^{-1}	Na^+	K^+	Ca^{2+}	Mg^{2+}	$SiO_2(aq)$	Na^+	K^+	Ca^{2+}	Mg^{2+}	$SiO_2(aq)$
1	3420	1.6	42.1	8.5	46.2	8.3	9.4	73.1	8.7	46.0	13.6	6.2
2	2319	4.3	27.8	8.1	14.0	5.8	13.1	195.3	33.3	56.2	38.6	35.3
3	2888	4.2	326.2	4.1	62.4	14.0	13.2	1,777.2	13.0	195.1	72.1	27.5
4	2898	17.1	29.6	9.9	12.0	5.5	13.0	655.6	128.4	152.1	116.1	110.0
5	1061	24.6	89.1	10.1	28.4	8.1	13.9	7,745.5	516.9	1,415.1	667.9	464.2
6	1654	6.7	13.7	4.1	13.1	3.9	10.2	209.1	36.8	114.7	57.1	59.6
7	5934	35.3	8.7	2.5	5.6	1.8	7.6	194.2	32.4	72.4	38.2	65.0
8	3666	377.0	23.6	2.4	6.5	1.7	6.3	9077.4	545.4	1440.9	621.6	931.7
9	7869	471.7	46.5	2.45	10.31	2.52	6.5	10425.6	324.5	1332.3	537.1	560.3
10	4966	66.8	6.3	1.6	4.0	0.9	5.8	316.1	47.8	115.3	41.0	111.3
11	4443	82.9	17.8	2.0	3.2	0.9	3.4	1,248.2	82.5	128.1	56.7	91.0
12	3803	44.6	3.9	1.4	2.4	0.5	4.2	173.0	37.2	59.4	20.6	70.4
13	3376	55.2	3.7	1.7	1.9	0.5	3.9	226.0	60.7	68.0	30.6	91.0
14	2681	-	-	-	-	-	-	-	-	-	-	-
15	3360	128.8	2.9	1.6	1.8	0.7	5.3	411.6	133.0	146.7	89.9	294.5
16	4840	132.7	2.1	1.6	2.0	0.5	4.0	218.5	95.0	120.4	49.9	156.0
17	4041	-	-	-	-	-	-	-	-	-	-	-
18	3493	30.7	6.0	1.1	1.8	0.6	3.3	198.9	21.5	34.3	20.0	42.0
19	3878	232.6	6.5	1.4	2.6	0.7	3.8	1,456.7	181.9	333.4	146.3	324.1
Mun [1]	70589	2543.1	9.0	1.9	5.0	1.1	4.6	1,220.0	149.9	390.5	145.0	237.3

[1] The entire Mun River watershed data.

3.5.2 Seasonal variability in mineral weathering and biomass degradation rates

Mineral weathering rates exhibit significant seasonal variability across the Mun River watershed (Table 5, Figure 6). During the dry season, weathering rates ranged from 0.15 to 497.4 μmol m^{-2} d^{-1}, with the highest rates observed in samples 13 and 9. In the wet season, weathering rates increased markedly, reaching up to 1,671.40 μmol m^{-2} d^{-1} in sample 5 and exceeding 1,000 μmol m^{-2} d^{-1} in subwatersheds 3, 5, and 9. This increase is

attributed to intensified hydrological processes and enhanced water-rock interactions driven by higher precipitation during the wet season. Geological factors, particularly the presence of feldspar, garnet, and halite—minerals highly susceptible to chemical weathering—play a substantial role in these processes, with halite dissolving rapidly and significantly contributing to dissolved ion fluxes. Spatial variability reflects the watershed's heterogeneous geological characteristics, with northern and central subwatersheds (samples 3, 5, and 9) showing particularly high rates. ANOVA results confirm a significant seasonal effect on mineral weathering rates ($p = 0.0009$).

Table 5. Seasonal mineral weathering and biomass degradation rates.

	Mineral weathering rate (μmol m^{-2} d^{-1})		**Biomass degradation rate (μmol m^{-2} d^{-1})**	
Sample	**Dry**	**Wet**	**Dry**	**Wet**
1	15.17	79.3	27.35	100
2	15.34	135.4	12.65	98
3	10.33	895.2	10.02	885.3
4	0.15	370.2	100	316.4
5	10.48	1,671.40	10.02	6,286.50
6	1.37	154.4	10.08	115.1
7	1.67	163.7	10	100
8	85.34	410.44	118.99	603.06
9	183.2	881.06	255.42	1294.54
10	0.63	270.6	9.92	108.7
11	15	646.5	10	612.6
12	17.82	166.4	10.62	99.6
13	497.4	183.6	483.74	109.6
14	-	-	-	-
15	23.42	333.6	25.3	182.9
16	16.59	193.3	10.37	115
17	-	-	-	-
18	14	142	11.78	100
19	21.98	808.2	18.33	687.2

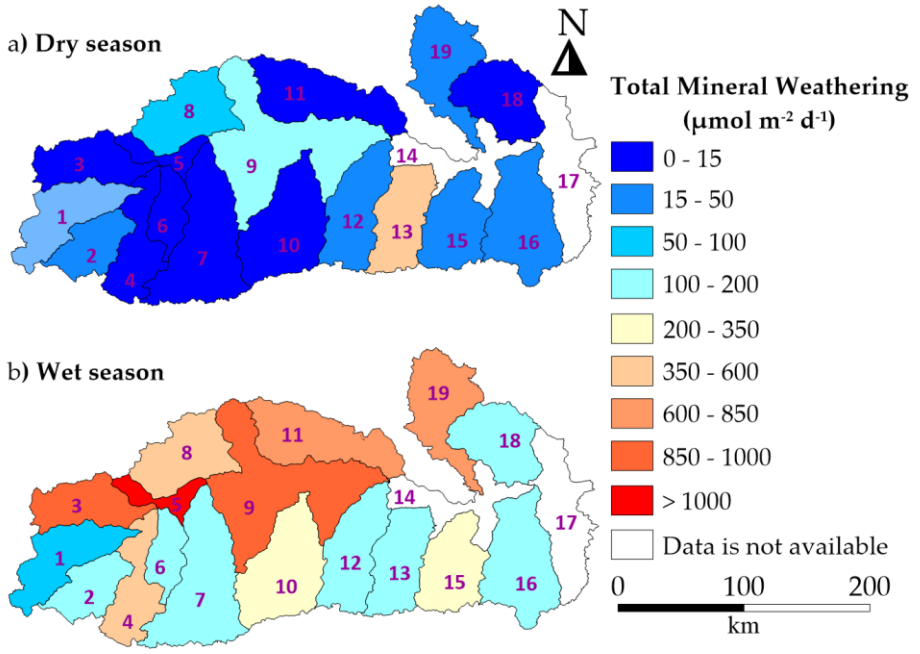

Figure 6. Total mineral weathering rates during dry and wet seasons.

Biomass degradation rates also demonstrated seasonal differences (Table 5, Figure 7). In the dry season, degradation rates ranged from 9.92 to 483.74 μmol m^{-2} d^{-1}, peaking in sample 13. During the wet season, degradation rates increased substantially, exceeding 1,000 μmol m^{-2} d^{-1} in subwatersheds 5 and 9, with a maximum of 6,286.50 μmol m^{-2} d^{-1} in sample 5. This increase is driven by enhanced microbial activity and organic matter inputs from agricultural runoff and land-use changes during the monsoon period. Higher flow rates and nutrient influx further promote biomass breakdown. Subwatersheds with extensive agricultural practices, such as 5, 9, and 8, exhibited the most pronounced increases, reflecting the influence of human activities on watershed biogeochemistry. ANOVA results indicate a modest seasonal effect on biomass degradation rates ($p = 0.0915$).

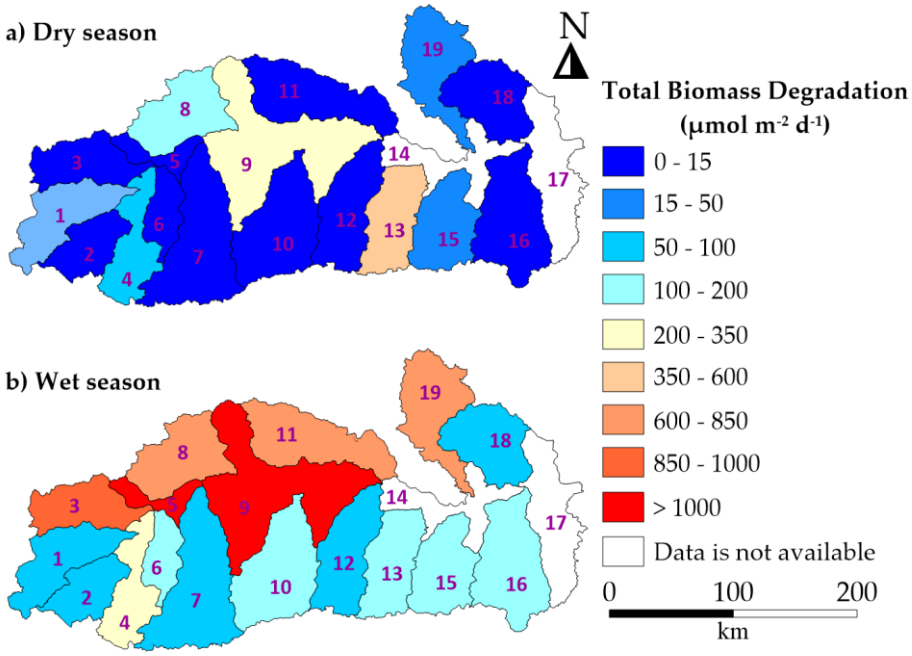

Figure 7. Biomass degradation rates during dry and wet seasons.

3.5.3 Seasonal and spatial variations in weathering and biomass degradation rates

The GMB results (Table 6) indicate that both mineral weathering and biomass degradation rates are significantly higher during the wet season compared to the dry season. Halite, quartz, and feldspar exhibited the highest weathering rates, with halite's high solubility contributing prominently to the overall rate. The total mineral weathering rate, calculated as the sum of rates (α_1–α_6) for major rock-forming minerals (quartz, halite, feldspar, garnet, biotite, and vermiculite), underscores the influence of geological composition on dissolution processes. Similarly, the biomass degradation rate (α_7) quantifies the contribution of organic material breakdown to dissolved ion fluxes.

The stoichiometric contributions of key cations (Na^+, Mg^{2+}, Ca^{2+}, K^+) from biomass decomposition were expressed using the formula $Na_xMg_yCa_zK_w$, where coefficients x, y, z, and w represent their relative contributions. These coefficients, along with weathering rates, were determined using the GMB method, integrating field-measured fluxes with stoichiometric data derived from XRD analyses and refined through PEST optimization techniques. This comprehensive approach enabled the simultaneous quantification of mineral weathering and biomass degradation for each subwatershed.

Table 6. Geochemical mass balance results for seasonal mineral weathering and biomass degradation

a). Dry season

Sample	Biomass Formula: $Na_xMg_yCa_zK_w$				Mineral Weathering Rates (µmol m^{-2} d^{-1})						Total Mineral Weathering (µmol m^{-2} d^{-1})	Biomass Degradation (µmol m^{-2} d^{-1})
	x	y	z	w	α_1	α_2	α_3	α_4	α_5	α_6		α_7
1	0.99	0.28	1.00	0.17	3.02	12.15	0.00	0.00	0.00	0.00	15.17	27.35
2	1.00	0.25	0.32	0.32	2.58	12.75	0.00	0.00	0.00	0.00	15.34	12.65
3	0.79	0.07	0.17	0.02	0.25	10.08	0.00	0.00	0.00	0.00	10.33	10.02
4	0.00	0.00	0.00	0.00	0.02	0.13	0.00	0.00	0.00	0.00	0.15	100.00
5	0.77	0.14	0.23	0.11	0.41	10.08	0.00	0.00	0.00	0.00	10.48	10.02
6	0.12	0.06	0.11	0.03	0.37	1.00	0.00	0.00	0.00	0.00	1.37	10.08
7	0.27	0.07	0.15	0.04	0.65	1.03	0.00	0.00	0.00	0.00	1.67	10.00
8	1.00	0.06	0.19	0.02	0.00	262.86	5.68	0.00	0.00	0.00	85.34	118.99
9	1.00	0.06	0.19	0.02	0.00	262.86	5.68	0.00	0.00	0.00	183.20	255.42
10	0.00	0.01	0.04	0.00	0.00	0.61	0.00	0.00	0.02	0.00	0.63	9.92
11	0.01	0.06	0.14	0.15	1.00	10.00	1.00	1.00	1.00	1.00	15.00	10.00
12	1.00	0.09	0.53	0.19	5.79	10.69	0.00	0.00	0.88	0.46	17.82	10.62
13	1.00	0.11	0.24	0.11	0.00	470.13	27.27	0.00	0.00	0.00	497.40	483.74
14	-	-	-	-	-	-	-	-	-	-	-	-

15	0.98	0.56	1.00	0.75	5.56	11.44	5.62	0.80	0.00	0.00	23.42	25.30
16	0.42	0.37	1.00	0.82	6.30	10.04	0.24	0.00	0.00	0.00	16.59	10.37
17	-	-	-	-	-	-	-	-	-	-	-	-
18	1.00	0.13	0.14	0.05	2.14	11.86	0.00	0.00	0.00	0.00	14.00	11.78
19	0.99	0.11	0.19	0.03	3.51	18.47	0.00	0.00	0.00	0.00	21.98	18.33
Mun [1]	1.00	0.37	1.00	0.21	0.00	75.38	5.79	0.00	0.00	0.00	81.17	50.66
Average	0.70	0.18	0.44	0.18								

[1] The entire Mun River watershed data.

a). Wet season

Sample	**Biomass Formula:** $Na_xMg_yCa_zK_w$				**Mineral Weathering Rates (μmol m^{-2} d^{-1})**						**Total Mineral Weathering (μmol m^{-2} d^{-1})**	**Biomass Degradation (μmol m^{-2} d^{-1})**
	x	y	z	w	α_1	α_2	α_3	α_4	α_5	α_6		α_7
1	0.00	0.14	0.46	0.09	6.2	73.1	0.0	0.0	0.0	0.0	79.3	100.0
2	0.97	0.39	0.57	0.34	35.3	100.1	0.0	0.0	0.0	0.0	135.4	98.0
3	1.00	0.08	0.22	0.01	0.0	884.9	10.3	0.0	0.0	0.0	895.2	885.3
4	1.00	0.37	0.45	0.41	20.3	316.4	33.5	0.0	0.0	0.0	370.2	316.4
5	1.00	0.11	0.22	0.08	178.2	1,386.5	106.7	0.0	0.0	0.0	1,671.4	6,286.5
6	0.99	0.50	1.00	0.32	59.6	94.8	0.0	0.0	0.0	0.0	154.4	115.1
7	0.94	0.38	0.72	0.32	63.0	100.0	0.8	0.0	0.0	0.0	163.7	100.0
8	1.00	0.10	0.24	0.09	294.0	997.6	0.0	0.0	0.0	0.0	410.44	603.06
9	1.00	0.10	0.24	0.09	294.0	997.6	0.0	0.0	0.0	0.0	881.06	1294.54
10	1.00	0.38	1.00	0.44	56.7	193.5	20.4	0.0	0.0	0.0	270.6	108.7
11	1.00	0.09	0.19	0.13	0.0	612.6	34.0	0.0	0.0	0.0	646.5	612.6
12	0.72	0.21	0.59	0.37	64.4	99.8	2.2	0.0	0.0	0.0	166.4	99.6
13	1.00	0.28	0.59	0.55	64.0	109.6	10.1	0.0	0.0	0.0	183.6	109.6
14	-	-	-	-	-	-	-	-	-	-	-	-
15	1.00	0.38	0.69	0.68	66.3	182.9	66.2	0.0	7.4	10.7	333.6	182.9
16	0.99	0.28	1.00	0.76	66.8	94.4	13.8	4.5	6.9	7.0	193.3	115.0
17	-	-	-	-	-	-	-	-	-	-	-	-
18	0.99	0.20	0.34	0.21	42.0	100.0	0.0	0.0	0.0	0.0	142.0	100.0
19	1.00	0.21	0.43	0.26	0.0	687.2	120.9	0.0	0.0	0.0	808.2	687.2
Mun [1]	1.00	0.25	0.62	0.26	0.0	579.9	88.5	0.0	0.0	0.0	668.4	579.9
Average	0.96	0.26	0.58	0.31								

[1] The entire Mun River watershed data.

Spatially, higher mineral weathering and biomass degradation rates were observed in the northern part of the Mun River watershed compared to the southern regions. This variability is primarily attributed to the easily weathered Maha Sarakham Formation and intensive agricultural land use in the north, which enhance water-rock interactions and biomass decomposition. These findings underscore the critical influence of climatic variability, land use, and geological characteristics on biogeochemical processes within the watershed.

3.6 Discussion of contour maps and geologic influences and agricultural factors

3.6.1 Spatial distribution of dissolved species and physicochemical parameters

Contour maps (Figure 8) illustrate the spatial distribution of dissolved cations, anions, and key physicochemical parameters (DO, conductivity, pH, temperature, and flow rate) within the Mun River watershed across dry and wet seasons. These maps highlight significant seasonal and spatial variability in dissolved species concentrations and water quality, shaped by hydrological conditions and geological settings.

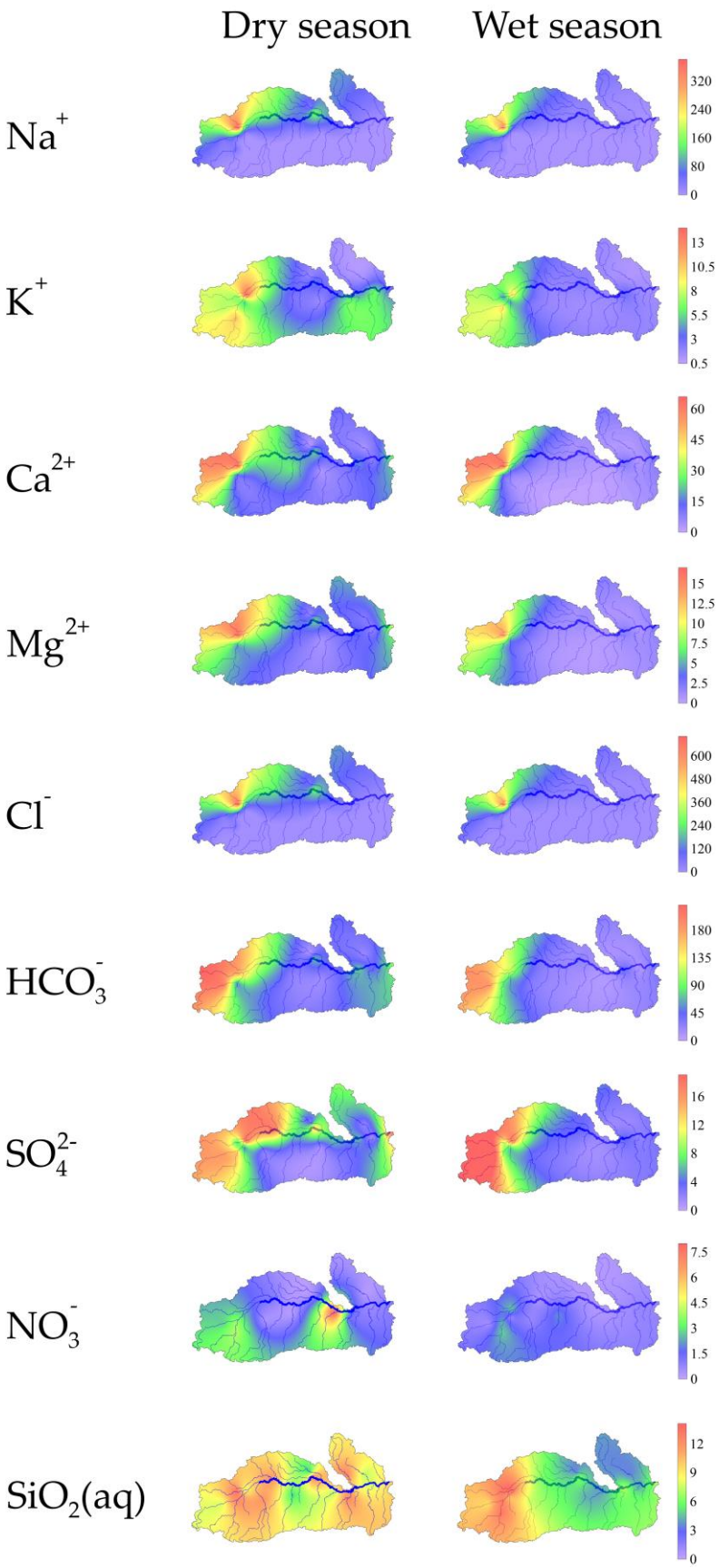

Figure 8. Contour maps of concentrations of dissolved cations and anions during the dry and wet seasons. All scale bars are in units of mg L^{-1}.

Dissolved species, such as Na^+, Cl^-, and SO_4^{2-}, show pronounced seasonal variability, with higher concentrations during the dry season due to evaporation and reduced discharge. In particular, Na^+ and Cl^- levels are elevated in the northern subwatersheds, attributed to evaporite dissolution from the Maha Sarakham Formation, a major source of surface salt [57]. This geological influence is evident in areas underlain by evaporite-rich lithology, where localized high levels of dissolved species are observed. Meanwhile, the upstream and western parts of the watershed, with lower annual precipitation [45], are more drought-prone, further concentrating dissolved species compared to downstream and eastern areas with higher rainfall [2,17].

The contour maps also reveal elevated Ca^{2+} and HCO_3^- concentrations in upstream regions, resulting from carbonate rock dissolution. Calcite supersaturation in tributaries, such as the Takhong River, highlights localized carbonate influences [55]. In contrast, the wet season's monsoonal rains dilute dissolved species concentrations across the watershed. Southern subwatersheds, affected by precipitation and runoff, experience particularly significant reductions in dissolved ion levels. However, regions overlying carbonate formations, such as the Khok Kruat Formation, display stable HCO_3^- concentrations across seasons, reflecting the buffering capacity of carbonate minerals in moderating seasonal fluctuations.

SO_4^{2-} and NO_3^- exhibit distinct spatial patterns. Elevated SO_4^{2-} levels in northern subwatersheds during both seasons suggest contributions from evaporite dissolution and agricultural runoff. Localized increases in SO_4^{2-} in southern subwatersheds are linked to agricultural practices, underscoring the dual influence of geology and land use on water quality within the watershed.

Contour maps of DO, conductivity, pH, temperature, flow rate, and TDS (Figure 9) further reveal seasonal dynamics:

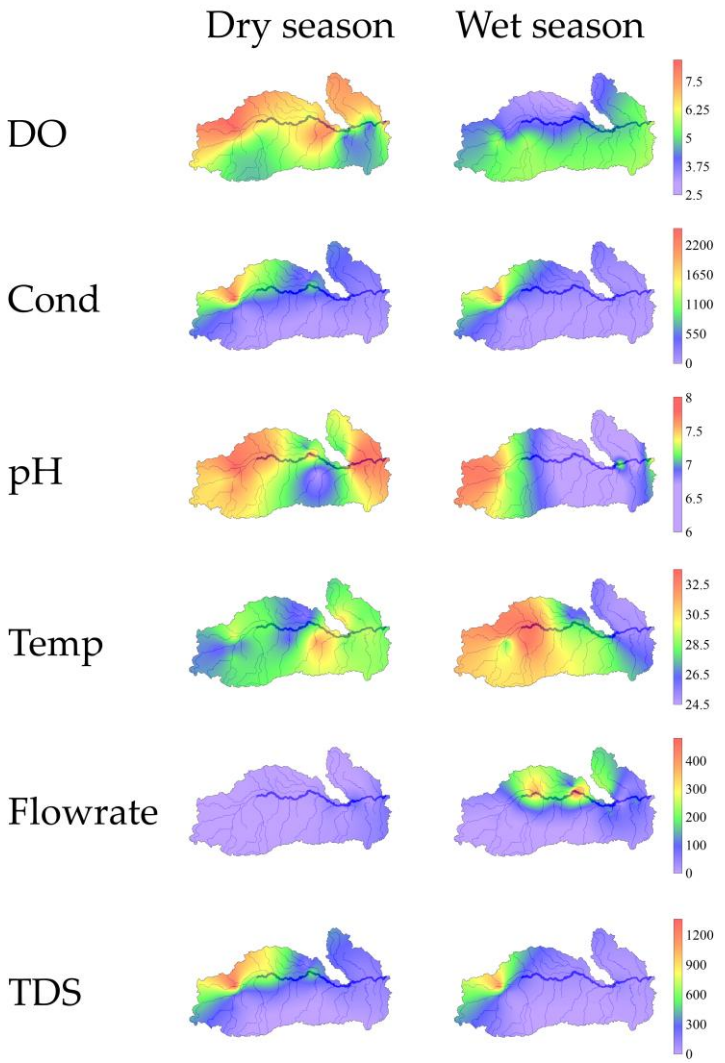

Figure 9. Contour maps of physicochemical parameters during the dry and wet seasons: dissolved oxygen (DO, mg L^{-1}), conductivity (µS/cm), pH (unitless), temperature (°C), and flowrate (m^3 s^{-1}) and total dissolved solids (TDS, mg L^{-1}).

- Dissolved oxygen (DO): Higher DO levels during the dry season, particularly in northern subwatersheds, are associated with organic material input and reduced flow. During the wet season, DO levels decline due to increased microbial activity and decomposition processes. Spatially, DO remains highest in upstream areas with natural aeration and lower nutrient runoff. Downstream areas, such as Ubon Ratchathani, show consistently reduced DO levels due to anthropogenic impacts and natural gradients [45].
- **Conductivity:** Conductivity is higher during the dry season, reflecting concentrated dissolved ions from evaporation and low water flow. In the wet season, rainfall dilutes ion concentrations across the watershed. Spatially, conductivity remains highest in areas underlain by highly soluble bedrock, showing the interplay between geology and seasonal hydrology.
- **pH:** Seasonal pH variation indicates higher alkalinity in the dry season due to reduced dilution and contributions from alkaline geological formations. During the wet season, pH shifts toward neutrality, especially in middle and lower reaches, due to dilution. Upstream tributaries draining carbonate formations, such as the Takhong River, sustain elevated pH levels across seasons, highlighting the buffering role of carbonate minerals [55].

- **Temperature:** Water temperature shows minimal seasonal variation, with slightly higher averages during the dry season. Spatially, temperature is relatively uniform but marginally higher in open, less vegetated regions with increased solar exposure. Groundwater inflows help moderate temperature fluctuations [46].
- **Flow rate:** Wet season flow rates rise dramatically due to monsoonal rainfall, diluting dissolved substances and enhancing oxygen distribution. Conversely, dry season flow rates are lower, leading to ion concentration and higher temperatures in stagnant areas.
- **Total dissolved solids (TDS):** TDS levels are higher during the dry season due to evaporation and reduced flow, with particularly elevated levels in northern subwatersheds influenced by geological formations and agricultural runoff. Wet season rains dilute TDS concentrations across the watershed, aligning with seasonal shifts in other physicochemical parameters.

3.6.2 Contour maps of dissolved species fluxes

Concentration contour maps alone do not fully capture the influence of processes like agricultural activities within the watershed, as they omit the role of flow rate. To address this, net export fluxes for dissolved solutes were calculated by incorporating flow rate, which is critical for accurately depicting spatial variations in solute transport. The resulting flux data (Table 7) and seasonal box plots (Figure 10) reveal distinct seasonal patterns, highlighting the hydrological control on biogeochemical processes.

Table 7. Seasonal flux statistics of major dissolved ions in the Mun River (μmol m^{-2} d^{-1}). P-values were calculated using a two-sample t-test (or Mann-Whitney U test for non-normal distributions) to assess seasonal differences, with a significance threshold of $p < 0.05$.

Parameter	Season	Min	Max	Mean	Median	SD[1]	p-value
Na^+	Dry	0.11	2716.85	419.63	23.65	785.59	0.001
	Wet	0.00	17971.18	2044.28	286.03	4378.72	
K^+	Dry	0.00	252.15	30.80	2.88	65.64	0.003
	Wet	0.00	556.74	121.13	47.86	165.76	
Ca^{2+}	Dry	0.00	1456.98	171.56	4.03	421.61	0.001
	Wet	0.00	2285.57	323.61	113.96	584.88	
Mg^{2+}	Dry	0.00	788.52	77.12	2.54	198.56	0.003
	Wet	0.00	921.04	143.07	56.37	245.88	
Cl^-	Dry	0.11	2206.43	404.12	22.71	712.29	0.003
	Wet	0.00	18905.60	2069.60	222.37	4565.26	
HCO_3^-	Dry	0.01	3433.52	435.96	19.51	1066.09	0.001
	Wet	0.00	4946.36	828.19	295.32	1360.18	
NO_3^-	Dry	0.00	155.63	10.57	0.01	36.04	0.003
	Wet	0.00	84.98	17.26	7.00	22.83	
SO_4^{2-}	Dry	0.00	400.91	37.88	0.83	97.68	0.001
	Wet	0.00	570.70	85.74	22.77	148.85	
$SiO_2(aq)$	Dry	0.01	402.66	54.24	3.02	120.32	0.001

Wet	0.00	961.27	179.44	90.96	242.64

[1]SD: Standard Deviation; p-values show significant seasonal differences at $p < 0.05$.

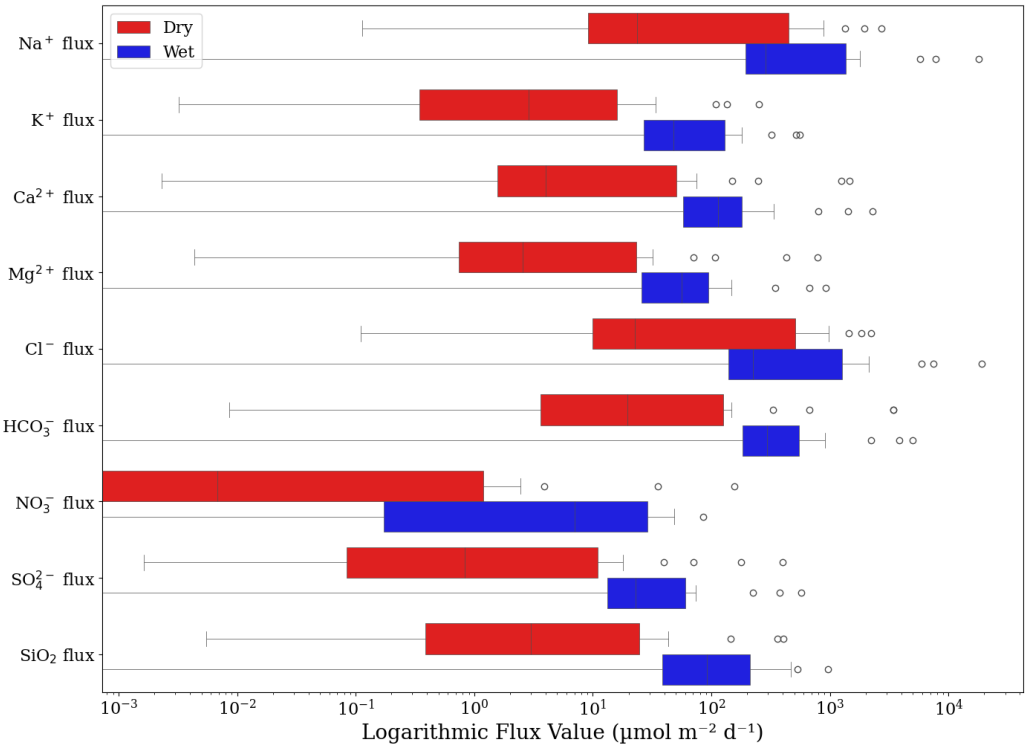

Figure 10. Seasonal box plots of fluxes of major dissolved species during the dry and wet seasons in the Mun River (logarithmic scale, µmol m^{-2} d^{-1}).

The flux contour maps (Figure 11) illustrate seasonal and spatial distribution, with significant increases observed during the wet season compared to the dry season. Fluxes of dissolved species, including nitrate, are most elevated in middle to northern subwatersheds, corresponding with areas experiencing the highest flow rates (as shown in the flow rate contour map). This pattern underscores water flow as a primary driver of seasonal solute transport, influencing weathering and biomass degradation across the watershed. Seasonal climatic changes further amplify the fluxes of dissolved species, particularly nitrogen, which exhibits marked variability between wet and dry seasons [58]. Increased fertilizer application during the wet season also contributes to nutrient loading [59].

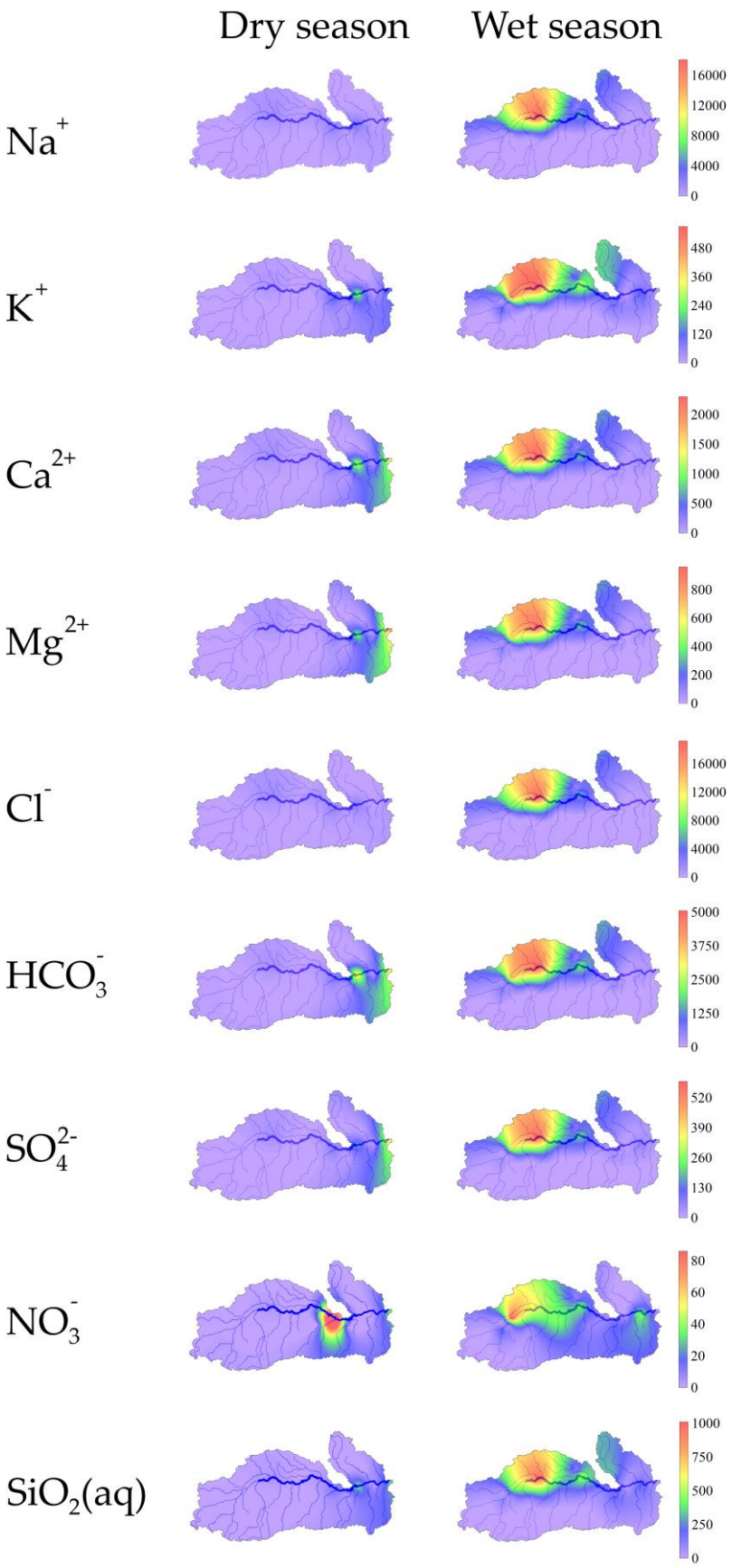

559

Figure 11. Contour maps of seasonal fluxes of major dissolved species during the dry and wet seasons in the Mun River (μmol m^{-2} d^{-1}). 560 561

The findings align with prior studies that identified runoff, lithology, and land cover as major determinants of bicarbonate fluxes and atmospheric CO_2 consumption in North American watersheds [23]. Similarly, bicarbonate fluxes in the Mun River respond strongly to seasonal flow variations and geological characteristics. The mean HCO_3^- flux increases from 435.96 μmol m^{-2} d^{-1} in the dry season to 828.19 μmol m^{-2} d^{-1} in the wet season, highlighting the critical role of flow rate in enhancing carbonate weathering and atmospheric CO_2 consumption during high-flow periods.

Specific dissolved species such as K^+, Na^+, Cl^-, NO_3^-, and SO_4^{2-} are closely linked to agricultural fertilizers, animal waste, and sewage. Sharp increases in Cl^-, NO_3^-, and SO_4^{2-} fluxes are observed in midstream areas, likely due to fertilizer use [46]. Similarly, elevated dissolved rare earth elements (REEs) in middle reaches, primarily attributed to agricultural fertilizers and sewage discharge, corroborate these patterns [60]. Although minimal, pesticide levels also peak during the wet season, reflecting increased agricultural runoff and its cumulative impact on water quality [45]. These hotspots of dissolved species fluxes, particularly in midstream northern subwatersheds, underscore the strong influence of agricultural activities.

Land use patterns vary across the watershed, with the northern subwatersheds and upstream Mun River dominated by agriculture, while southern subwatersheds are more forested [45]. Agricultural watersheds discharge significantly higher nutrient loads than forested ones [61,62]. Nitrate flux, often associated with runoff contaminants like pesticides, peaks during wet seasons, exacerbating water quality and aquatic ecosystem impacts [63].

Statistical analysis of fluxes reveals significant seasonal differences for all measured dissolved species, in contrast to concentration data alone. This highlights the importance of incorporating flow rate—a critical hydrological factor—into flux calculations to accurately capture dissolved solute transport. Representing solute fluxes rather than concentrations provides a clearer depiction of biogeochemical processes, particularly in areas influenced by agricultural activities.

4. Conclusions

This study provides a comprehensive assessment of seasonal biogeochemical variations in the Mun River watershed, highlighting the interplay of hydrological, geological, and anthropogenic factors in shaping water quality. Seasonal shifts in hydrochemical facies, from Na-Cl dominance in the dry season to Ca-HCO_3 in the wet season, are primarily driven by changes in flow rates, dilution, and mineral weathering. The Geochemical Mass Balance (GMB) method quantified significant spatial and seasonal variability in mineral weathering and biomass degradation rates, with northern subwatersheds exhibiting the highest values due to intensive agriculture and reactive lithology. Contour maps and flux analyses underscore water availability as a critical factor influencing solute transport and nutrient cycling, with elevated fluxes during the wet season driven by increased precipitation and runoff. Anthropogenic influences, including agricultural runoff and wastewater discharge, exacerbate water quality issues, necessitating targeted management strategies. Future research should use advanced techniques like Principal Component Analysis (PCA) to disentangle the contributions of hydrology, geology, and human activity, supporting adaptive watershed management to ensure sustainable water quality and ecosystem health amidst climate change and intensified land use.

Supplementary Materials: The following supporting information can be downloaded at: www.mdpi.com/xxx/s1, Figure S1: title; Table S1: title; Video S1: title.

Author Contributions: For research articles with several authors, a short paragraph specifying their individual contributions must be provided. The following statements should be used "Conceptualization, X.X. and Y.Y.; methodology, X.X.; software, X.X.; validation, X.X., Y.Y. and Z.Z.; formal

analysis, X.X.; investigation, X.X.; resources, X.X.; data curation, X.X.; writing—original draft preparation, X.X.; writing—review and editing, X.X.; visualization, X.X.; supervision, X.X.; project administration, X.X.; funding acquisition, Y.Y. All authors have read and agreed to the published version of the manuscript." Please turn to the CRediT taxonomy for the term explanation. Authorship must be limited to those who have contributed substantially to the work reported.

Funding: Please add: "This research received no external funding" or "This research was funded by NAME OF FUNDER, grant number XXX" and "The APC was funded by XXX". Check carefully that the details given are accurate and use the standard spelling of funding agency names at https://search.crossref.org/funding. Any errors may affect your future funding.

Data Availability Statement: We encourage all authors of articles published in MDPI journals to share their research data. In this section, please provide details regarding where data supporting reported results can be found, including links to publicly archived datasets analyzed or generated during the study. Where no new data were created, or where data is unavailable due to privacy or ethical restrictions, a statement is still required. Suggested Data Availability Statements are available in section "MDPI Research Data Policies" at https://www.mdpi.com/ethics.

Acknowledgments: In this section, you can acknowledge any support given which is not covered by the author contribution or funding sections. This may include administrative and technical support, or donations in kind (e.g., materials used for experiments).

Conflicts of Interest: The authors declare no conflicts of interest. The funders had no role in the design of the study; in the collection, analyses, or interpretation of data; in the writing of the manuscript; or in the decision to publish the results.

References

1. Bridhikitti, A.; Prabamroong, T.; Yu, G. Problem identification on surface water quality in the Mun River Basin, Thailand. *Sustainable Water Resources Management* **2020**, *6*, 53, DOI https://doi.org/10.1007/s40899-020-00413-8.
2. Prabnakorn, S.; Maskey, S.; Suryadi, F.X.; de Fraiture, C. Assessment of drought hazard, exposure, vulnerability, and risk for rice cultivation in the Mun River Basin in Thailand. *Nat Hazards* **2019**, *97*, 891–911, DOI http://dx.doi.org/10.1007/s11069-019-03681-6.
3. Babel, M.S.; Chawrua, L.; Khadka, D.; Tingsanchali, T.; Shanmungam, M.S. Agricultural drought risk and local adaptation measures in the Upper Mun River Basin, Thailand. *Agric Water Manage* **2024**, *292*, 108655, DOI http://dx.doi.org/10.1016/j.agwat.2023.108655.
4. Wang, J.; Lu, X.X.; Kummu, M. Sediment load estimates and variations in the Lower Mekong River. *River Research and Applications* **2011**, *27*, 33–46, DOI https://doi.org/10.1002/rra.1337.
5. Khadka, D.; Babel, M.S.; Kamalamma, A.G. Assessing the impact of climate and land-use changes on the hydrologic cycle using the SWAT Model in the Mun River Basin in Northeast Thailand. *Water* **2023**, *15*, 3672, DOI https://doi.org/10.3390/w15203672.
6. Kosa, P.; Sukwimolseree, T. Effect of climate change on runoff in the Upper Mun River Basin, Thailand. *International Journal of Environmental and Ecological Engineering* **2014**, *8*, 423–427.
7. Ziv, G.; Baran, E.; Nam, S.; Rodríguez-Iturbe, I.; Levin, S.A. Trading-off fish biodiversity, food security, and hydropower in the Mekong River Basin. *Proceedings of the National Academy of Sciences* **2012**, *109*, 5609–5614, DOI http://dx.doi.org/10.1073/pnas.1201423109.
8. Hecht, J.S.; Lacombe, G.; Arias, M.E.; Dang, T.D.; Piman, T. Hydropower dams of the Mekong River basin: A review of their hydrological impacts. *Journal of hydrology* **2019**, *568*, 285–300, DOI http://dx.doi.org/10.1016/j.jhydrol.2018.10.045.
9. Li, R.; Huang, H.; Yu, G.; Yu, H.; Bridhikitti, A.; Su, T. Trends of runoff variation and effects of main causal factors in Mun River, Thailand during 1980–2018. *Water* **2020**, *12*, 831, DOI http://dx.doi.org/10.3390/w12030831.
10. Pingmuanglek, P.; Jakrawatana, N.; Gheewala, S.H. Freshwater use analysis of cassava for food feed fuel in the Mun River basin, Thailand. *The International Journal of Life Cycle Assessment* **2017**, *22*, 1705–1717, DOI http://dx.doi.org/10.1007/s11367-017-1286-y.
11. Prabnakorn, S.; Suryadi, F.X.; Chongwilaikasem, J.; De Fraiture, C. Development of an integrated flood hazard assessment model for a complex river system: a case study of the Mun River Basin, Thailand. *Modeling Earth Systems and Environment* **2019**, *5*, 1265–1281, DOI http://dx.doi.org/10.1007/s40808-019-00634-7.
12. Prabnakorn, S.; Ruangpan, L.; Tangdamrongsub, N.; Suryadi, F.X.; de Fraiture, C. Improving flood and drought management in agricultural river basins: an application to the Mun River Basin in Thailand. *Water Policy* **2021**, *23*, 1153–1169, DOI http://dx.doi.org/10.1007/s40808-019-00634-7.
13. Zhao, Z.; Liu, G.; Liu, Q.; Huang, C.; Li, H. Studies on the spatiotemporal variability of river water quality and its relationships with soil and precipitation: A case study of the Mun River Basin in Thailand. *International journal of environmental research and public health* **2018**, *15*, 2466, DOI http://dx.doi.org/10.3390/ijerph15112466.
14. Khadka, D.; Babel, M.S.; Collins, M.; Shrestha, S.; Virdis, S.G.; Chen, A.S. Projected changes in the near-future mean climate and extreme climate events in northeast Thailand. **2021**, DOI http://dx.doi.org/10.1002/joc.7377.
15. Liu, M.; Han, G.; Li, X. Using stable nitrogen isotope to indicate soil nitrogen dynamics under agricultural soil erosion in the Mun River basin, Northeast Thailand. *Ecol Ind* **2021**, *128*, 107814, DOI http://dx.doi.org/10.1016/j.ecolind.2021.107814.

16. Artlert, K.; Chaleeraktrakoon, C. Modeling and analysis of rainfall processes in the context of climate change for Mekong, Chi, and Mun River Basins (Thailand). *Journal of hydro-environment research* **2013**, *7*, 2–17, DOI http://dx.doi.org/10.1016/j.jher.2013.01.001.
17. Bridhikitti, A.; Ketuthong, A.; Prabamroong, T.; Renzhi, L.; Jing, L.; Gaohuan, L. Forecasting 100-year changes of streamflow in the Mun River Basin (NE Thailand) under the HAPPI experiment using the SWAT model. *Journal of Water and Climate Change* **2022**, *13*, 1706–1724, DOI http://dx.doi.org/10.2166/wcc.2022.358.
18. Li, C.; Fang, H. Assessment of climate change impacts on the streamflow for the Mun River in the Mekong Basin, Southeast Asia: Using SWAT model. *Catena* **2021**, *201*, 105199, DOI http://dx.doi.org/10.1016/j.catena.2021.105199.
19. Li, S.; Liu, C.; Li, J.; Lang, Y.; Ding, H.; Li, L. Geochemistry of dissolved inorganic carbon and carbonate weathering in a small typical karstic catchment of Southwest China: Isotopic and chemical constraints. *Chem Geol* **2010**, *277*, 301–309, DOI http://dx.doi.org/10.1016/j.chemgeo.2010.08.013.
20. Oliva, P.; Viers, J.; Dupré, B. Chemical weathering in granitic environments. *Chem Geol* **2003**, *202*, 225–256, DOI http://dx.doi.org/10.1016/j.chemgeo.2002.08.001.
21. West, A.J.; Galy, A.; Bickle, M. Tectonic and climatic controls on silicate weathering. *Earth Planet Sci Lett* **2005**, *235*, 211–228, DOI http://dx.doi.org/10.1016/j.epsl.2005.03.020.
22. Millot, R.; Gaillardet, J.; Dupré, B.; Allègre, C.J. The global control of silicate weathering rates and the coupling with physical erosion: new insights from rivers of the Canadian Shield. *Earth Planet Sci Lett* **2002**, *196*, 83–98, DOI http://dx.doi.org/10.1016/s0012-821x(01)00599-4.
23. Moosdorf, N.; Hartmann, J.; Lauerwald, R.; Hagedorn, B.; Kempe, S. Atmospheric CO2 consumption by chemical weathering in North America. *Geochim Cosmochim Acta* **2011**, *75*, 7829–7854, DOI http://dx.doi.org/10.1016/j.gca.2011.10.007.
24. Zhao, Z.; Liu, K.; Yu, B.; Liu, G.; Wang, Y.; Wu, C. Modeling of agricultural nonpoint-source pollution quantitative assessment: a case study in the mun river basin, Thailand. *Sustainability* **2023**, *15*, 10325, DOI http://dx.doi.org/10.3390/su151310325.
25. Zhao, Z.; Liu, G.; Liu, Q.; Huang, C.; Li, H.; Wu, C. Distribution characteristics and seasonal variation of soil nutrients in the Mun River Basin, Thailand. *International journal of environmental research and public health* **2018**, *15*, 1818, DOI http://dx.doi.org/10.3390/ijerph15091818.
26. Sukwimolseree, T.; Kosa, P. The relationship between land use change and runoff. *International Journal of Environmental and Ecological Engineering* **2014**, *8*, 428–431.
27. Tian, H.; Yu, G.; Tong, L.; Li, R.; Huang, H.Q.; Bridhikitti, A.; Prabamroong, T. Water quality of the Mun river in Thailand—Spatiotemporal variations and potential causes. *International journal of environmental research and public health* **2019**, *16*, 3906, DOI http://dx.doi.org/10.3390/ijerph16203906.
28. Yadav, S.; Babel, M.S.; Shrestha, S.; Deb, P. Land use impact on the water quality of large tropical river: Mun River Basin, Thailand. *Environ Monit Assess* **2019**, *191*, 614, DOI http://dx.doi.org/10.1007/s10661-019-7779-3.
29. Han, G.; Yang, K.; Zeng, J.; Zhao, Y. Dissolved iron and isotopic geochemical characteristics in a typical tropical river across the floodplain: The potential environmental implication. *Environ Res* **2021**, *200*, 111452, DOI http://dx.doi.org/10.1016/j.envres.2021.111452.
30. Han, G.; Liu, M.; Li, X.; Zhang, Q. Sources and geochemical behaviors of rare earth elements in suspended particulate matter in a wet-dry tropical river. *Environ Res* **2023**, *218*, 115044, DOI http://dx.doi.org/10.1016/j.envres.2022.115044.
31. Floch, P.; Molle, F.; Loiskandl, W. Marshalling water resources: a chronology of irrigation development in the Chi-Mun River Basin, Northeast Thailand. *Colombo, Sri Lanka: CGIAR Challenge Program on Water and Food* **2007**.

32. PCD Development of an action plan to improve the water quality in the northeastern basin, Thailand. *Mun Basin Data, Annex I: Part 3, 10(C.3)* **1995**.
33. Liu, J.; Han, G.; Liu, X.; Liu, M.; Song, C.; Zhang, Q.; Yang, K.; Li, X. Impacts of anthropogenic changes on the Mun River water: insight from spatio-distributions and relationship of C and N species in Northeast Thailand. *International Journal of Environmental Research and Public Health* **2019**, *16*, 659, DOI http://dx.doi.org/10.3390/ijerph16040659.
34. Binnie; Partners *Mun river basin water resources development master plan. Technical Report*, Royal Irrigation Department.: 1995;.
35. Harriman, R.; Morrison, B.; Caines, L.A.; Collen, P.; Watt, A.W. Long-term changes in fish populations of acid streams and lochs in Galloway south west Scotland. *Water Air Soil Pollut* **1987**, *32*, 89–112, DOI http://dx.doi.org/10.1007/bf00227686.
36. Reynolds, B.; Stevens, P.A.; Hughes, S.; Parkinson, J.A.; Weatherley, N.S. Stream chemistry impacts of conifer harvesting in Welsh catchments. *Water Air Soil Pollut* **1995**, *79*, 147–170, DOI http://dx.doi.org/10.1007/bf01100435.
37. Li, H.; Fu, D.; Huang, C.; Su, F.; Liu, Q.; Liu, G.; Wu, S. An approach to high-resolution rice paddy mapping using time-series Sentinel-1 SAR data in the Mun River Basin, Thailand. *Remote Sensing* **2020**, *12*, 3959, DOI http://dx.doi.org/10.3390/rs12233959.
38. Park, S.; Im, J.; Park, S.; Yoo, C.; Han, H.; Rhee, J. Classification and mapping of paddy rice by combining Landsat and SAR time series data. *Remote Sensing* **2018**, *10*, 447, DOI http://dx.doi.org/10.3390/rs10030447.
39. Phalke, A.R.; Özdoğan, M. Large area cropland extent mapping with Landsat data and a generalized classifier. *Remote Sens Environ* **2018**, *219*, 180–195, DOI http://dx.doi.org/10.1016/j.rse.2018.09.025.
40. Velbel, M.A.; Price, J.R. Solute geochemical mass-balances and mineral weathering rates in small watersheds: Methodology, recent advances, and future directions. *Appl Geochem* **2007**, *22*, 1682–1700, DOI http://dx.doi.org/10.1016/j.apgeochem.2007.03.029.
41. Zhang, S.; Han, G.; Zeng, J.; Xiao, X.; Malem, F. A strontium and hydro-geochemical perspective on human impacted tributary of the Mekong River Basin: sources identification, fluxes, and CO2 consumption. *Water* **2021**, *13*, 3137, DOI http://dx.doi.org/10.3390/w13213137.
42. Penny, J.; Alves, P.B.; De-Silva, Y.; Chen, A.S.; Djordjević, S.; Shrestha, S.; Babel, M. Analysis of potential nature-based solutions for the Mun River Basin, Thailand. *Water Science & Technology* **2023**, *87*, 1496–1514, DOI http://dx.doi.org/10.2166/wst.2023.050.
43. Toda, O.; Tanji, H.; Somura, H.; Higuchi, K.; Yoshida, K. Evaluation of tributaries contribution in the Mekong River Basin during rainy and dry season. **2004**, 239–248, DOI http://dx.doi.org/10.1007/s10333-005-0015-5.
44. Prabnakorn, S.; Maskey, S.; Suryadi, F.X.; de Fraiture, C. Rice yield in response to climate trends and drought index in the Mun River Basin, Thailand. *Sci Total Environ* **2018**, *621*, 108–119, DOI http://dx.doi.org/10.1016/j.scitotenv.2017.11.136.
45. Akter, A.; Babel, M.S. Hydrological modeling of the Mun River basin in Thailand. *Journal of Hydrology* **2012**, *452*, 232–246, DOI http://dx.doi.org/10.1016/j.jhydrol.2012.05.059.
46. Li, X.; Han, G.; Liu, M.; Song, C.; Zhang, Q.; Yang, K.; Liu, J. Hydrochemistry and dissolved inorganic carbon (DIC) cycling in a tropical agricultural river, Mun River Basin, Northeast Thailand. *International Journal of Environmental Research and Public Health* **2019**, *16*, 3410, DOI http://dx.doi.org/10.3390/ijerph16183410.
47. Akter, A.; Babel, M.S. Water quality of Mun river, Thailand, Proceedings of the International Conference on Environmental Science and Technology, 2005; , pp. 44–49.

48. Chomcheawchan, P.; Pawana, V.; Julphunthong, P.; Kamdee, K.; Laonamsai, J. Innovative Assessment of Mun River Flow Components through ANN and Isotopic End-Member Mixing Analysis. *Geosciences* **2024**, *14*, 150, DOI http://dx.doi.org/10.20944/preprints202403.1843.v1.
49. Taylor, A.B.; Velbel, M.A. Geochemical mass balances and weathering rates in forested watersheds of the southern Blue Ridge II. Effects of botanical uptake terms. *Geoderma* **1991**, *51*, 29–50, DOI http://dx.doi.org/10.1016/0016-7061(91)90065-2.
50. Plummer, N.; Back, W. The mass balance approach: application to interpreting the chemical evolution of hydrologic systems. *Am J Sci* **1980**, *280*, 130–142, DOI http://dx.doi.org/10.2475/ajs.280.2.130.
51. Liang, B.; Han, G.; Liu, M.; Li, X.; Song, C.; Zhang, Q.; Yang, K. Spatial and temporal variation of dissolved heavy metals in the Mun River, Northeast Thailand. *Water* **2019**, *11*, 380, DOI http://dx.doi.org/10.3390/w11020380.
52. World Health Organization Guidelines for drinking-water quality. *WHO Chron* **2011**, *38*, 104–108.
53. Liu, J.; Han, G. Tracing riverine sulfate source in an agricultural watershed: Constraints from stable isotopes. *Environmental Pollution* **2021**, *288*, 117740, DOI http://dx.doi.org/10.1016/j.envpol.2021.117740.
54. Zhang, S.; Han, G.; Zeng, J.; Malem, F. Source tracing and chemical weathering implications of strontium in agricultural basin in Thailand during flood season: A combined hydrochemical approach and strontium isotope. *Environ Res* **2022**, *212*, 113330, DOI http://dx.doi.org/10.1016/j.envres.2022.113330.
55. Li, X.; Han, G.; Liu, M. Seasonal and Spatial Variations of δ13CDIC Values in the Mun River, Northeast Thailand. *Water* **2022**, *14*, 1340, DOI http://dx.doi.org/10.3390/w14091340.
56. Doherty, J. PEST model-independent parameter estimation user manual. *Watermark Numerical Computing, Brisbane, Australia* **2004**, *3338*, 3349.
57. Wongsomsak, S. Salinization in northeast Thailand. *Japanese Journal of Southeast Asian Studies* **1986**, *24*, 133–153, DOI https://doi.org/10.20495/tak.24.2_133.
58. Correll, D.L.; Jordan, T.E.; Weller, D.E. Transport of nitrogen and phosphorus from Rhode River watersheds during storm events. *Water Resour Res* **1999**, *35*, 2513–2521, DOI http://dx.doi.org/10.1029/1999wr900058.
59. Bridhikitti, A.; Prabamroong, T.; Liu, G.; Yu, G. Best management practices for mitigating agricultural nutrient pollution in the Mun River Basin, Thailand. *Soil & Water Research* **2021**, *16*, DOI http://dx.doi.org/10.17221/101/2020-swr.
60. Ma, S.; Han, G.; Yang, Y.; Li, X. Agricultural activity on the Mun River basin: insight from spatial distribution and sources of dissolved rare earth elements in northeast Thailand. *Environmental Science and Pollution Research* **2023**, *30*, 106736–106749, DOI http://dx.doi.org/10.1007/s11356-023-29917-4.
61. Beaulac, M.N.; Reckhow, K.H. An examination of land use-nutrient export relationships 1. *JAWRA Journal of the American Water Resources Association* **1982**, *18*, 1013–1024, DOI http://dx.doi.org/10.1111/j.1752-1688.1982.tb00109.x.
62. Vanni, M.J.; Renwick, W.H.; Headworth, J.L.; Auch, J.D.; Schaus, M.H. Dissolved and particulate nutrient flux from three adjacent agricultural watersheds: a five-year study. *Biogeochemistry* **2001**, *54*, 85–114, DOI http://dx.doi.org/10.1023/a:1010681229460.
63. Williams, R.J.; Brooke, D.N.; Matthiessen, P.; Mills, M.; Turnbull, A.; Harrison, R.M. Pesticide transport to surface waters within an agricultural catchment. *Water and Environment Journal* **1995**, *9*, 72–81, DOI http://dx.doi.org/10.1111/j.1747-6593.1995.tb00928.x.